



ELSEVIER

Contents lists available at ScienceDirect

Nuclear Instruments and Methods in Physics Research A

journal homepage: www.elsevier.com/locate/nima

Experimental characterization of the Advanced Liquid Hydrogen Cold Neutron Source spectrum of the NBSR reactor at the NIST Center for Neutron Research



J.C. Cook^{a,*}, J.G. Barker^a, J.M. Rowe^a, R.E. Williams^a, C. Gagnon^b, R.M. Lindstrom^c,
R.M. Ibberson^a, D.A. Neumann^a

^a NIST Center for Neutron Research, National Institute of Standards and Technology, 100 Bureau Drive, Mail Stop 6100, Gaithersburg, MD 20899-6100, USA

^b Department of Materials Science and Engineering, University of Maryland, College Park, MD 20742, USA

^c Scientist Emeritus, Chemical Sciences Division, National Institute of Standards and Technology, 100 Bureau Drive, Mail Stop 8395, Gaithersburg, MD 20899-8395, USA

ARTICLE INFO

Article history:

Received 9 February 2015

Received in revised form

13 April 2015

Accepted 14 April 2015

Available online 30 April 2015

Keywords:

Liquid hydrogen

Cold neutron sources

Neutron moderators

Research reactors

Neutron guides

Radiation transport calculations

ABSTRACT

The recent expansion of the National Institute of Standards and Technology (NIST) Center for Neutron Research facility has offered a rare opportunity to perform an accurate measurement of the cold neutron spectrum at the exit of a newly-installed neutron guide. Using a combination of a neutron time-of-flight measurement, a gold foil activation measurement, and Monte Carlo simulation of the neutron guide transmission, we obtain the most reliable experimental characterization of the Advanced Liquid Hydrogen Cold Neutron Source brightness to date. Time-of-flight measurements were performed at three distinct fuel burnup intervals, including one immediately following reactor startup. Prior to the latter measurement, the hydrogen was maintained in a liquefied state for an extended period in an attempt to observe an initial radiation-induced increase of the ortho (o)-hydrogen fraction. Since para (p)-hydrogen has a small scattering cross-section for neutron energies below 15 meV (neutron wavelengths greater than about 2.3 Å), changes in the o- p hydrogen ratio and in the void distribution in the boiling hydrogen influence the spectral distribution. The nature of such changes is simulated with a continuous-energy, Monte Carlo radiation-transport code using 20 K o and p hydrogen scattering kernels and an estimated hydrogen density distribution derived from an analysis of localized heat loads. A comparison of the transport calculations with the mean brightness function resulting from the three measurements suggests an overall o- p ratio of about 17.5(±1) % o- 82.5% p for neutron energies < 15 meV, a significantly lower ortho concentration than previously assumed.

Published by Elsevier B.V.

1. Introduction

Cold neutron sources greatly enhance the scope of materials research and isotope yield capabilities of research and test reactors. They shift the neutron spectrum from a thermal equilibrium dictated by the core/bulk moderator temperature (a thermal Maxwellian with effective temperature of around 320 K in the case of the NBSR reactor at NIST) to one which enhances the intensity of lower energy (longer wavelength) neutrons. The spectral shift is achieved by establishing localized regions of cryogenically-cooled moderator. After Butterworth et al. built the first cold neutron device in a nuclear reactor (BEPO at Harwell, UK) in 1957 [1,2] cold neutron sources were incorporated into the design of both nuclear reactor-based, steady-state neutron sources (including the use of liquid hydrogen isotopes) [3,4] and of pulsed neutron sources [5]. High brightness (neutron flux per unit solid angle) cold neutron sources using liquid deuterium were very

successfully implemented at the Institut Laue-Langevin in the 1970s and 1980s [6,7], with similar concepts at the FRM-II, Technische Universität München, Garching, Germany [8] and the Opal Reactor in Australia [9]. More compact cold sources, using liquid hydrogen, have been successfully operated at the Orphée reactor, France, the HFIR reactor at Oak Ridge National Laboratory, USA, and here at the NIST Center for Neutron Research (NCNR).

The source brightness function is sensitively dependent on the moderator material, volume, shape, temperature, and pressure of operation. The Advanced Liquid Hydrogen Cold Neutron Source (“Unit 2”) at the NBSR NIST research reactor is the third-generation cold source at the facility and is the second to use liquid hydrogen at 20 K and atmospheric pressure [10].

Hydrogen molecules exhibit angular momentum states characterized by rotational quantum number J . The low-temperature equilibrium corresponds to relaxation of all molecules into the lowest energy ($J=0$) state. As a result, molecules with even angular momentum (para-hydrogen) have a small scattering cross-section, unless the neutron energy is sufficient (> 15 meV) to allow excitation to a

* Corresponding author.

higher angular momentum state. On the other hand, molecules with odd J (ortho-hydrogen) have a large scattering cross-section for all neutron energies. At elevated temperatures, the ratio of ortho to para hydrogen reflects the thermally-populated degeneracy of the triplet ($m_J = -1, 0, +1$) ortho $J=1$ state to the singlet $J=0$ para state, and consequently tends towards 75% o- 25% p, sometimes referred to as “normal” hydrogen. The all $J=0$ para ground state in liquid hydrogen is rarely achieved without catalysis. The Unit 2 cold source does not employ catalysis, since increasing the para- H_2 fraction is actually detrimental to the neutron intensity in the most valued neutron energy range below 5 meV (neutron wavelengths greater than about 4 Å) for this design. However, J-PARC in Japan uses a moderator which employs a catalyst to produce hydrogen largely in the p-state [11], and the European Spallation Source, to be built in Sweden, plans to employ a moderator system which will use nearly 100% para- H_2 [12]. It is worth noting, however, that in an operating neutron source, radiation-induced molecular dissociation always introduces some ortho-hydrogen into the moderator even if the hydrogen was prepared in the para-state prior to start-up.

In the absence of a measurement, the cold neutron source spectrum may be estimated using transport codes. A challenge of this approach is achieving a correct characterization of the low temperature state of the materials, which also depends on the reliability of the scattering kernels at the operating temperature and pressure of the cold source. For boiling liquid hydrogen at 20 K, the scattering cross-section depends on the ortho-para hydrogen ratio and on the void distribution in the boiling liquid. In this work, we have investigated the hydrogen o- p ratio dependence with the MCNP6 transport code [13] using ENDF/B-VII.0 [14] continuous energy o and p hydrogen scattering kernels ($T=20$ K). For these simulations, the liquid hydrogen density distribution was estimated from an analysis of localized heat load per unit mass of LH_2 , normalized to a measured mean void fraction (obtained from mockup tests [15]) of 18%.

The “cold neutrons” are typically conducted many tens of meters from the reactor core to external instrumentation using hollow, neutron-reflective guide tubes, whose entrances are close to the cold moderator. Following an idea by Heinz Maier Leibnitz and some early proofs of principle, the first totally reflecting neutron guides [16,17] were developed, which increase the solid angle of collection of the source neutrons and conduct them efficiently towards instruments that may be sited some tens of meters away. Many improvements have been made to the technology since, including high quality substrate preparation and the development of “supermirrors” [18,19 and references therein]. Neutron guides are in widespread use and are the backbone of the recent expansion of the facilities at the NCNR [20].

The availability of an end-position on a new neutron guide offered a rare opportunity to perform a controlled measurement of the NBSR Unit 2 cold neutron source spectrum. The method consisted of measuring the spectrum at the guide exit via the neutron time-of-flight (TOF) technique, then relating it to the source spectrum via Monte Carlo simulation of the neutron guide transmission. The intensity was normalized using a gold foil activation measurement. The available neutron guide (NG-Bu) is suited on several counts: The initial 23 m are curved, excluding direct lines of sight between the source and the guide exit. Consequently, the emerging spectrum is relatively free of fast neutron and gamma ray contamination. Such a guide design exhibits a rapid reduction in neutron transmission for wavelengths, λ , below a certain characteristic wavelength, λ_c [21–23]. Despite this, the relatively short characteristic wavelength, λ_c , of the curved section of NG-Bu (about 3.2 Å) allowed the spectrum to be measured reliably for wavelengths down to about 0.8 Å (energies up to about 150 meV). Finally, the majority of reflecting surfaces are coated with high reflectivity natural nickel. The high Fresnel-law reflectivity of the Ni coatings reduces significantly the simulated transmission uncertainty associated with reflections from these surfaces. The remaining surfaces (those of the outer radius of the curved

section) are coated with $m=1.5^1$ supermirror. The $m=1.5$ reflectivity could be modeled more accurately than is customary owing to the availability of measured reflectivity profiles, each of which could be correlated with a specific reflecting surface of a specific guide element. Additionally, the relatively low m causes the solid angle of guide acceptance to remain within the cavity region of the source to longer wavelengths than is achievable for a similar guide with high m coatings. This simplifies the interpretation of the brightness function for λ below about 12 Å (see Section 5).

2. Cold neutron source and the NG-Bu neutron guide geometry

The liquid hydrogen cold neutron source is illustrated in Fig. 1. Fig. 1(a) shows a cutaway view through the heavy concrete biological shielding that reveals the reactor core and fuel elements, thimble, cryostat vessel, and in-pile neutron guides. Fig. 1(b) and (c) shows horizontal and vertical cuts, respectively, though the MCNP model of the cold source assembly. The NG-Bu guide is shown schematically in Fig. 2 (for clarity, the figure is plotted in a heavily distorted aspect ratio, which also falsifies the angles). Downstream of the in-pile guide section, the curved guide is a polygonal approximation to a pure curve of radius 1432.4 m, with nominally $m=1.5$ supermirror coatings on the outer radial surface and natural nickel on all other surfaces. The final section, coated with all natural nickel, is straight.

3. Experimental

The apparatus used for the TOF measurements is illustrated schematically in Fig. 3. The measurements were performed with a single-slotted chopper disk with rotational speed 4506.86 rpm (measured mean), which gave an optimal compromise between wavelength resolution (favoring a higher chopper speed) and white beam frame overlap (favoring a lower chopper speed). With an estimated flight path length, $D \approx 850.5$ mm (measured to the mid-plane of the fissile coatings of the LND-3053 fission chamber detector [10^{-3} nominal thermal neutron detection efficiency]) and a neutron pulse repetition period, τ , of 13,313 μ s, a wavelength frame length of about $h\tau/(m_n D) \approx 62$ Å is achieved, where h is Planck's constant and m_n is the neutron mass. The 62 Å wavelength is just beyond the point at which the measured signal becomes indistinguishable from the (very low) background level (no detectable slope of the TOF data plotted on a log intensity scale). Consequently, frame overlap corrections were eliminated and only a very low time-independent background level subtraction was necessary. Simulations performed using code written for this purpose [24], confirm that the TOF spectrum produced by two separated, but otherwise similar, thin (low interaction probability) fissile detector coatings is almost exactly that produced by a single fissile layer at the bisector. This is a good approximation even at long wavelength, where the resolution function separates into two distinct peaks (see Appendix C). The chopper-bisector separation (effective flight path length) is designated by the symbol $\langle D \rangle$. The 10^{-3} thermal neutron detection efficiency of the fission chamber detector gave an excellent compromise between reduced counting times and minimized dead-time distortion at the arrival of the spectral peak. The fission chamber also yielded extremely low gamma background and a “ $1/\nu$ ” response² that produced not only increased sensitivity to long wavelengths, but also a spectrum that could be directly normalized by the thermal-equivalent flux, φ_c , obtained from the gold foil activation

¹ Here m characterizes the ratio of the effective reflectivity cutoff in wave vector transfer with respect to that of natural nickel, such that the nickel critical angle defines $m=1$.

² “ $1/\nu$ ” refers to a response (in this case the detected signal intensity) that is inversely proportional to the incident neutron velocity (proportional to neutron wavelength).

measurement. The thermal-equivalent flux may be written as

$$\varphi_c = \frac{1}{\lambda_{2200}} \int_0^\infty \lambda \frac{d\varphi(\lambda)}{d\lambda} d\lambda \quad (1)$$

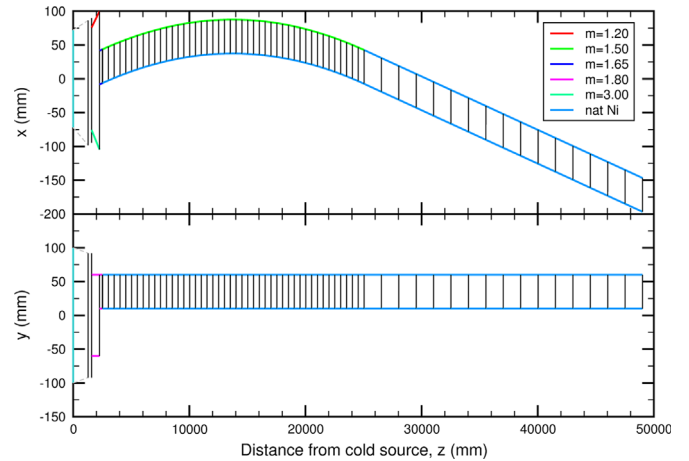
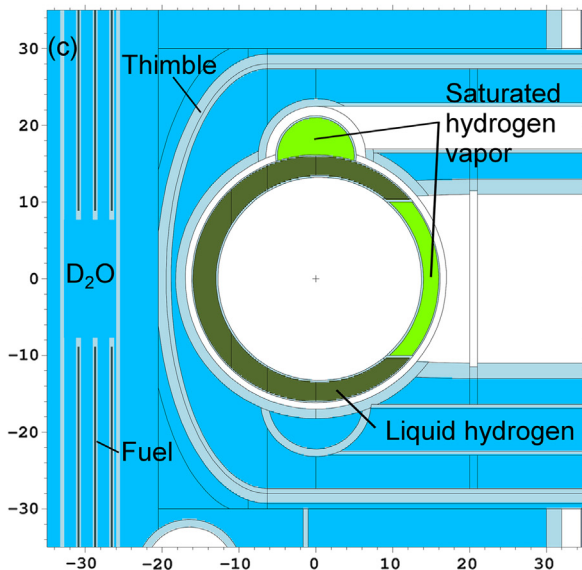
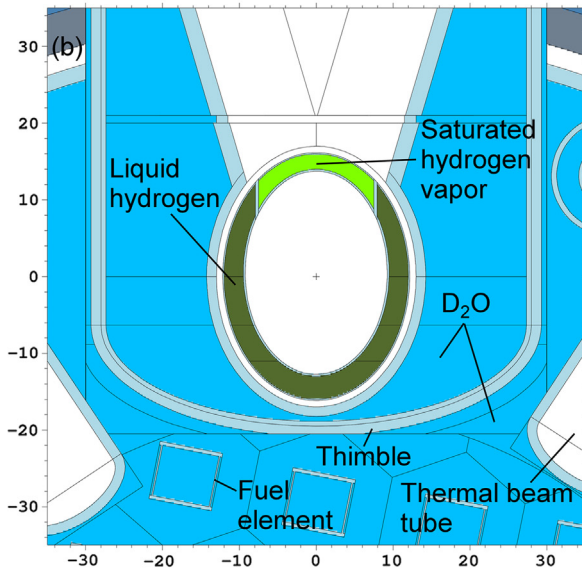
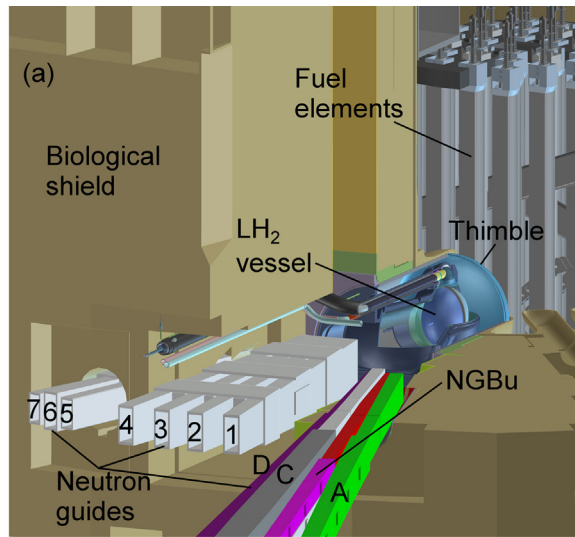


Fig. 2. A schematic of the NG-Bu guide from the center plane of the cold source liquid hydrogen vessel to the guide exit. Top: Plan view through the beam center plane. Bottom: Projected elevation view showing that the guide center is 3.5 cm above the vertical center of the cold source. The TOF apparatus used for the measurement was installed immediately downstream of the guide exit.

where, $d\varphi(\lambda)/d\lambda$ is the neutron flux per unit wavelength and λ_{2200} is the wavelength of a neutron traveling at a speed of $2200 \text{ ms}^{-1} = h/m_n$ [$\text{ms}^{-1} \text{ \AA}$]/2200 $\approx 1.798 \text{ \AA}$.

The epithermal neutron background was kept very low by having a full 1 mm thickness of cadmium on both the chopper disk and the entrance slit (0.5 mm was insufficiently opaque). Capture gamma radiation from the cadmium was greatly reduced by pre-masking the Cd entrance slit with a greater-than-beam-sized, 2 mm thick sheet of lithiated polymer (PNPI Lithoflex with $N(^6\text{Li}) \approx 3 \times 10^{22} \text{ cm}^{-3}$) containing a slightly oversized slit in such a way that the majority of stray neutron beam is captured in ^6Li (see Fig. 3). With 4096 time channels and a single-slotted disk, the time channel width (dwell time) was optimally set to $13,313/4096 = 3.25 \mu\text{s}$, which is an exact multiple of the discrete resolution of the Turbo MCS data acquisition system, hence the somewhat unusual chopper speed selection. Fine-tuning the chopper speed in this way avoided a significant dead region between the end of frame accumulation and the subsequent chopper trigger. The corresponding wavelength channel width is about $62/4096 \approx 0.015 \text{ \AA}$.

Because the position of the zero time of flight ($\lambda \rightarrow 0$) channel is, *a priori*, unknown to sufficient accuracy, two additional TOF transmission measurements were performed with room temperature polycrystalline beryllium and graphite crystals of about 4.8 cm and 7.6 cm thickness, respectively. These measurements established two wavelength reference positions from the positions of their Bragg edges. This information was used to provide both an accurate wavelength calibration and the magnitude of rotational data shift necessary to place the zero wavelength channel at the start of the spectrum (see Appendix A). An independent estimate of the effective flight path length, $\langle D \rangle$, is also obtained from this two-point calibration.

Three high-resolution TOF experiments were performed on and around Oct 24 2012, Nov 20 2012, and Dec 3, 2012 at various stages of the reactor cycle under the following conditions:

1. After an initial 13 days of reactor/cold source operation and a 2-day shutdown, the October measurements were performed on

Fig. 1. Views of the Unit2 liquid hydrogen cold source at the NBSR. In the left figure (a), the seven older guides, NG-1 to NG-7, (numbered 1 to 7) are shown to the left. The newer guides (identified by letters) emerge from the port to the right. The NG-B guide (second from the right) is split into an upper and lower guide. The upper portion (labeled NG-Bu), is the guide used for these measurements. The figures (b) and (c) are horizontal and vertical cuts respectively through the MCNP model in the vicinity of the liquid hydrogen vessel. The white regions are evacuated in the cold source cryostat and filled with CO_2 in the adjacent thermal beam thimbles.

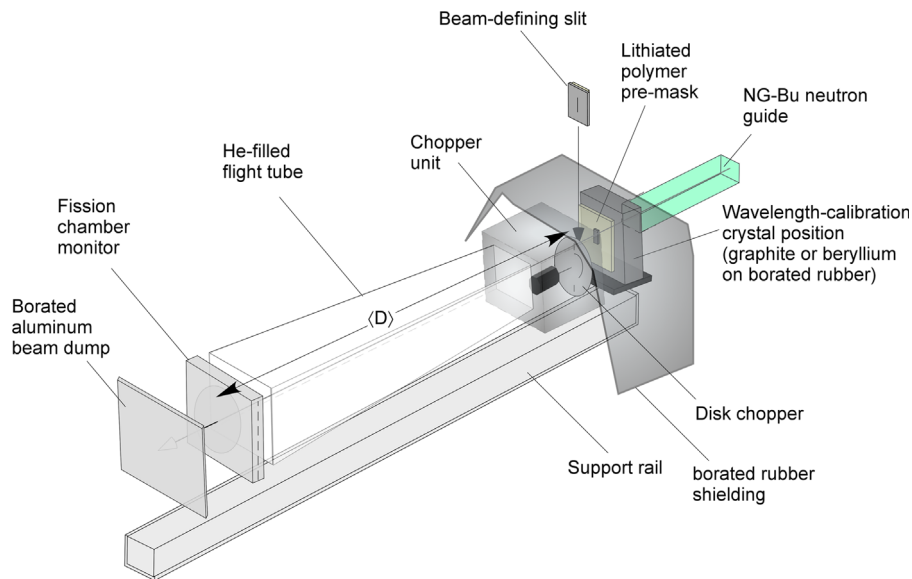


Fig. 3. A schematic of the apparatus used for the neutron time-of-flight measurement at the end of neutron guide NG-Bu.

the second day of subsequent 20 MW reactor power (the previous day having been interrupted by a 45-min refrigerator shutdown).

2. The November measurements were performed 4 days from the end of a fuel cycle with uninterrupted reactor/cold source operation – likely yielding an equilibrium o- p hydrogen ratio.
3. The December measurements were performed immediately following the start of a fresh fuel cycle, with the cold source para-hydrogen content as close to 100% as time permitted. In order to obtain maximum (uncatalyzed) relaxation of the liquid hydrogen into its ground state, the cold source refrigerator was run continuously for a number of days prior to reactor startup.

4. TOF data reduction

The data reduction may be summarized as follows:

1. Sum compatible TOF data sets (as necessary).
2. Normalize to count rate using total run duration (since no beam monitor was available).
3. Perform time-independent background subtraction – (the background level was determined by averaging approximately 100 channels occurring within the 62 Å to 0 Å wrap-around region).
4. Perform the wavelength/TOF calibration using the beryllium and graphite crystal data to determine the effective chopper-to-detector distance, $\langle D \rangle$, and the TOF delay δ preceding the zero TOF channel (see Appendix A).
5. Using the result for δ in step 4, perform a circular shift of the TOF data to align the zero TOF channel at the zero abscissa (to within a half-channel width accuracy [$< 0.0075 \text{ \AA}$]).
6. Perform the TOF-to-wavelength conversion via $\lambda = h/m_n \times \text{TOF} / \langle D \rangle$ for the shifted spectrum, using the value of $\langle D \rangle$ obtained from step 4.
7. Perform the resolution correction (see Appendix C).
8. Divide the resulting wavelength spectrum by the estimated λ -dependent transmission of the elements between the guide exit and the active part of detector. This corresponds to about 25.4 cm air, 68.6 cm He, and 0.0556 cm Al (2 aluminum foil windows 0.0024 cm thick each plus 1 detector window thickness 0.02" [0.0508 cm]).
9. Normalization of the spectrum from step 8 to an absolute intensity via the thermal-equivalent (capture) flux, φ_c [Eq. (1)], obtained from the gold foil irradiation at the exit of the neutron guide. Since the fission chamber response to thermal neutrons is "1/v", the spectrum at this stage is also 1/v-weighted (λ -weighted). Therefore, the normalization of the latter is performed simply by ensuring that its numerical integral is equal to φ_c . The resulting spectrum is the thermal-equivalent flux per unit wavelength, $d\varphi_c(\lambda)d\lambda$, in units of $\text{cm}^{-2} \text{ s}^{-1} \text{ \AA}^{-1}$. A 0.2" (0.51 cm) diameter gold foil, placed near the center of the guide cross-section, gave $\varphi_c = 2.34(3) \times 10^9 \text{ cm}^{-2} \text{ s}^{-1}$. The quoted error of about $\pm 1.4\%$ (1σ) is dominated by the foil irradiation time uncertainty, which, in turn, is caused by the duration of the beam shutter transit and the unknown fractional opening occurring between shutter "closed" and shutter "open" indicator status.
10. Remove the thermal-equivalent bias in $d\varphi_c/d\lambda$ via $d\varphi/d\lambda = d\varphi_c/d\lambda \times \lambda_{2200}/\lambda$, from Eq. (1).

The results of this analysis, including propagated errors (see Appendix D), are shown in Fig. 4.

5. Obtaining the source brightness from the end-of-guide spectrum

The measurements in Fig. 4 represent the spectrum at the exit of the neutron guide NG-Bu. In order to obtain the source brightness function, these data must be divided by the source-to-guide exit transmission function, for which no direct measurement exists. Therefore, the latter is obtained using Monte Carlo ray-tracing simulations [24]. The neutron guide transmission depends on the specific reflectivity and misalignment distributions of the as-installed guide elements. It is well known that the sputtered supermirror reflectivity, even that of relatively low m , is subject to an appreciable standard deviation (particularly between fabrication batches) of both the effective m (typically $\Delta m(1\sigma)/\langle m \rangle$ is between 1% and 3%) and of the value of the reflectivity at the position m (typically $\Delta R_1(1\sigma)/\langle R_1 \rangle$ is between 1% and 5%). For the NG-Bu guide, we are fortunate enough to possess measured supermirror reflectivity profiles associated with specific reflecting surfaces for many of the individual guide elements. In other cases,

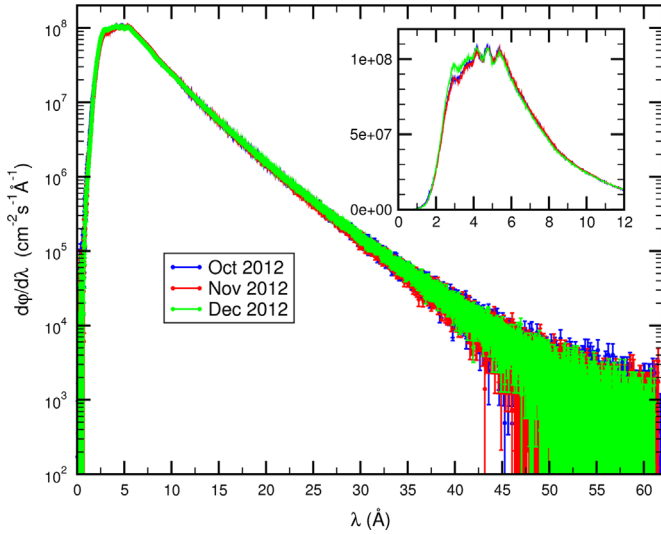


Fig. 4. Measured neutron flux per unit wavelength, $d\phi/d\lambda$, at the exit of NG-Bu resulting from the October, November, and December 2012 TOF measurements, as indicated in the legend. In the main figure, the curves are plotted on a log vertical scale showing a signal above background to beyond 60 Å wavelength. The origin of the error bars on these curves is fully described in Appendix D. The inset shows the same data (with symbols and error bars removed for clarity), plotted on a linear vertical scale and reduced wavelength scale to better reveal the spectral differences of the three measurements in the peak region.

reflectivity measurements characterizing guide elements produced from a given batch were available. Either way, knowing the installation sequence of guide elements, we have been able to replicate the actual supermirror reflectivity variations along the guide as closely as is practically possible. This decreases the systematic error associated with the reflectivity aspect of the simulation model in a way that is not usually achievable. Uncertainty in the distribution of m , for example, sensitively influences the short wavelength transmission “cut-off” position, whereas variations in R particularly influence the simulated long wavelength transmission, since this tends to rely on increasing numbers of reflections with increasing wavelength.

We turn to the interpretation of the source brightness in light of the constraints imposed on the guide simulation. The simulation uses a single, elliptically-shaped source region, whose dimensions ($a=7.5$ cm semi-minor width, $b=10$ cm semi-major height) correspond to the cold source cavity exit window limits (see Fig. 1). Neutrons are emitted uniformly from this region towards random points on the guide entrance, which is a good approximation in this case. The simulation is used to project what source brightness, $d^2\phi(\lambda)/d\lambda d\Omega$ (neutrons emitted per second per unit source area, A_s , per unit wavelength, per unit solid angle³), is necessary to reproduce the measured $d\phi(\lambda)/d\lambda$ at the guide exit. The resulting brightness function is thus subject to the imposed constraints of the physical source limits, of source uniformity, and of the assumed guide reflection characteristics. The Unit 2 cold source clearly extends laterally beyond the cavity window limits (Fig. 1) and some neutrons transmittable by the guide (particularly those of longer wavelength) originate from this outer region. A complication arises because the spectrum emitted from the outer region differs from that of the central cavity. Qualitatively, the spectral peak is shifted to longer wavelength and the longest wavelengths are suppressed by increased absorption. Because it is difficult to account for this spatial dependence when it is *a-priori* unknown, a single, uniform source

approach is adopted. If an extended source area were chosen, a different *effective* brightness function is produced, which averages the spectrum over the larger area and the guide transmission over a correspondingly wider range of neutron incident angles. Therefore, the source brightness function must be qualified in terms of the assumptions made about the source in the simulation. Nonetheless, if the compatible brightness function-source area combination is used in the simulation, statistically-equivalent results are achieved at the guide exit.

Fortunately, the complication of assigning different brightness functions to different source regions is more or less eliminated below a certain wavelength. Owing to the small angle reflection characteristics of a neutron guide, neutrons transmitted by a long guide originate from a restricted spatial-angular acceptance region at the source, dictated by the guide geometry, proximity of the guide entrance to the source, and the critical angle(s), $\theta_c(\lambda)$, of its reflective coatings. Since θ_c is proportional to the neutron wavelength, to a very good approximation, the “allowed” source region tends to grow with increasing wavelength, unless inhibited by a physical boundary. When the acceptance area falls beyond the source boundary, the guide is said to be “under-illuminated”. However, when simulating a source brightness from a *known* spectrum at the guide exit (i.e., the reverse of what is usually performed), an artificially-imposed source boundary will not reproduce under-illumination per se, but rather the estimated source brightness adjusts to compensate for the acceptance region lost outside of the boundary. For the particular case of NG-Bu with a cavity window-sized source, the simulated brightness and true exit window brightness should be more or less indistinguishable for wavelengths up to about 10 Å to 12 Å. This is because the small guide cross-section (5 cm × 5 cm), combined with the low critical angle (natural Ni) coatings, concentrate the acceptance area within the exit window region for this wavelength range. This is illustrated in Fig. 5 in which the origins of neutrons transmitted by the guide for several wavelengths are plotted. This wavelength range would be greater if the vertical center of the NG-Bu guide coincided with the vertical center of the source.

Apart from the reflectivity, the guide elements are subject to misalignment errors, dimensional errors (for example, of the entrance/exit dimensions, substrate parallelism, or deviation from intended angle, substrate waviness etc.). These are all subject to some distribution within specified manufacturing tolerances, in most cases. For most guide elements, these errors have been characterized by measurements. Misalignments associated with the installation were estimated from the accuracy of the alignment procedure [25]. The latter consists of: (i) fiducializing each guide element with multiple alignment “pucks”, (ii) measuring the mean axis of each element with respect to the fiducials with a portable coordinate measuring machine, and (iii) laying the element axis on the CAD-generated intended axis by positioning the element fiducials (henceforth of known relation to the element axis) along a reference determined by a building-wide network of fiducials, by means of a laser tracker. In the simulations, the misalignment distributions are assumed Gaussian. The lateral element-element misalignments in x and y have a full width at half maximum (FWHM) of approximately 0.01 mm (about the dimensional tolerance of the guide element), the element-to-element angular misalignments in x and y have a FWHM $\approx 4 \times 10^{-5}$ rads (based on our experience with standard 1.5 m long sections). Finally, the substrate waviness (which is the long-range variation of surface normal with respect to the nominal perpendicular) has a 1σ deviation $\approx 1 \times 10^{-4}$ rads (FWHM $\approx 2.35 \times 10^{-4}$ rads), which was the specified manufacturing tolerance. For all misalignment distributions, apart from waviness, the configuration randomness is selected once at the start of each simulation, then these aspects of the geometry are frozen. The waviness is applied at each reflection, assuming that the

³ The solid angle in this case is the perpendicular projection of the guide entrance area, A_s , at the source point, divided by the square of the source point to guide entrance point distance, d_{sg} . For large d_{sg} , such that trajectory angles are small with respect to the initial guide axis direction, the solid angle tends towards A_s/d_{sg}^2 .

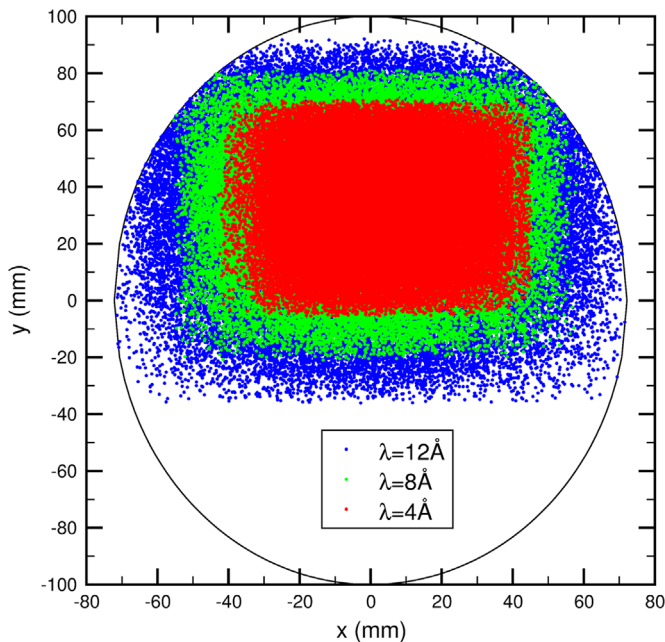


Fig. 5. Simulated origins of neutrons transmitted by the neutron guide NG-Bu, projected onto the elliptical cold source exit window region (indicated by the black elliptical outline). Overlapping patches are shown for neutrons with wavelength $\lambda=4$ Å (smallest area), $\lambda=8$ Å (intermediate area), and $\lambda=12$ Å (largest area). The apparent reduction of the semi-minor dimension (from the 75 mm nominal exit window dimension to 72.15 mm) is a consequence of the oblique viewing angle of the exit window from the NG-Bu guide entrance). The point density indicates the relative transmission probability of neutrons originating from that region. The 3.5 cm vertical displacement of the NG-Bu guide with respect to the source center (see Fig. 2) is also evident from the vertical offset of the points with respect to the center.

reflection points, separated by distances that are uncorrelated on the atomic length scale, sample the waviness distribution. The standard deviation of the guide transmission due to misalignments is estimated by performing many simulations with different random starting configurations (in this case 100). Individual simulations were performed with sufficiently high Monte Carlo statistics for the results to reflect the variation associated with the misalignments, rather than the statistical error. Fig. 6 shows a total of 300 simulations:– 100 simulations superimposed for each of the three $d\phi/d\lambda$ distributions obtained from the October, November, and December TOF measurements (see Fig. 4), where the largely misalignment-induced scatter is evident. In order to isolate the expected cavity brightness region (see discussion above), for which the results may be directly compared with transport calculations, the wavelength region up to $\lambda=12$ Å is plotted. The error bars on individual data sets are mainly due to the propagated uncertainties on $d\phi/d\lambda$ resulting from the analysis of the TOF measurements, combined with a comparatively small Monte Carlo statistical error. A detailed analysis of the experimental uncertainties is given in Appendix D. The 100 simulation-averaged brightness functions for each measurement, together with the average from all 300 simulations are shown in Fig. 7. Again, the error bars are a combination of statistical errors and standard deviations as outlined in Appendix D.

6. Discussion

Using the estimated liquid hydrogen density distribution described in Section 1, the best-fit MCNP simulation for neutron wavelengths greater than about 4 Å (neutron energy, $E_e < 5$ meV) is that shown in Fig. 7. The “best fit” criterion was established as follows: (i) The “measured” brightness curve (mean of all simulations

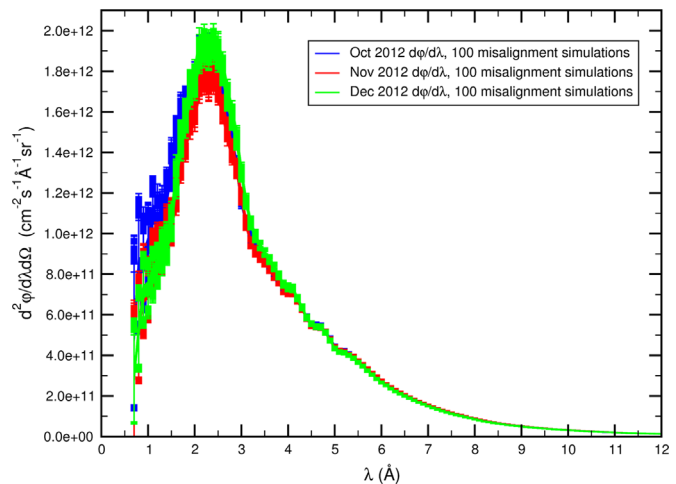


Fig. 6. Estimated source brightness functions derived from the three measured $d\phi/d\lambda$ spectra (Fig. 4) obtained from the October, November, and December 2012 TOF measurements, as indicated in the legend. For each measured $d\phi/d\lambda$ curve, the figure shows 100 brightness functions (superimposed), obtained from 100 simulations of the NG-Bu guide transmission with random misalignments selected from their assumed (Gaussian) distributions. Each brightness function reproduces $d\phi/d\lambda$ at the guide exit for its particular guide misalignment configuration, subject to the constraint that the source area falls within the cavity window region, as described in Section 5. This is expected to be close to the real situation for the plotted wavelength range up to 12 Å (see Fig. 5). The element-to-element lateral misalignments and angular misalignments were selected one-time at the start of the simulation with FWHM=0.01 mm and 4×10^{-5} rads, respectively, whereas the substrate waviness was selected with a $1\sigma=1 \times 10^{-4}$ rads (FWHM=2.35 $\times 10^{-4}$ rads) at each reflection point. The error bars on the individual simulation curves are those described by Eq. (16) in Appendix D. Note that symbols are turned off in this plot to more clearly illustrate the statistical scatter of the curves due to the guide misalignments.

combined – open black circles in Fig. 7) and the corresponding measurement uncertainties were interpolated onto the abscissa of the MCNP simulations (mean bin wavelengths), (ii) the interpolated measurement errors and the MCNP statistical errors were combined in quadrature, (iii) an effective χ^2 was calculated from the result. This process was repeated for wavelength ranges with $\lambda_{max}=12$ Å and $\lambda_{min}=2$ Å, 3 Å, 4 Å, and 5 Å. For $\lambda_{min} \geq 5$ Å, the best fit MCNP simulation assumes an ortho: para hydrogen ratio of about 18.5%: 81.5%. For $\lambda_{min}=2, 3, \text{ or } 4$, the best fit was obtained with a slightly lower ortho content ($\approx 16.5\%$ to 17.5%), both significantly below what has been previously assumed. The 17.5% ortho content provides the best overall agreement between the MCNP simulations and the measurements with respect to both the peak region of the spectrum ($E \approx 15$ meV, $\lambda \approx 2.3$ Å) and the long wavelength spectrum ($E < 3$ meV, $\lambda > 5.2$ Å). Qualitatively, lower ortho content simulations produce a taller peak and reduced long wavelength intensity, whereas higher ortho content produces a lower peak with increased long wavelength intensity. The feature differences observed between the beginning-of-cycle (December), 2-week (October), and the near end-of-cycle (November) results (see Section 3), shown in Figs. 4 and 7, cannot be explained in terms of variations in the o- p ratio, insofar as these variations are described by the MCNP6 simulations using ENDF B-VII.0 (ENDF71SaB library) kernels. The three measured spectra are almost identical beyond about 8 Å wavelength and the observed variations in the peak region with changing o- p content would be correlated with measurable differences at longer wavelength. For example, the November measurement peak is best described by the MCNP simulation with about 45% ortho content, but this leads to an intensity at $\lambda > 6$ Å which is too large to agree satisfactorily with the measurement. It is also difficult to speculate upon how this conclusion may change, if both the ortho and para kernels were to be modified in future updates of the nuclear data; thus within the framework of the currently known multiple uncertainties of our analysis, the spectral differences appear inconsistent with a simple

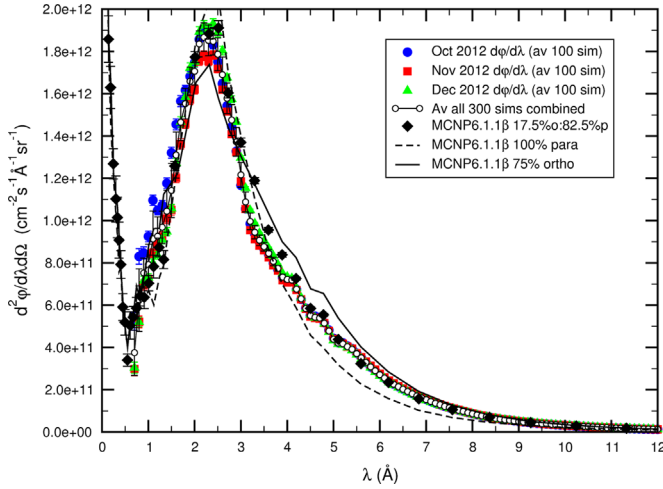


Fig. 7. Mean brightness functions derived from averages of the functions shown in Fig. 6. The averages specific to the October, November, and December $d\phi/d\lambda$ measurements (see Eq. (17), Appendix D) are represented by the full circles, squares, and triangles respectively. The uncertainty on each point (given by Eq. (20)) is a combination of the individual 1σ simulation errors contributing to the average, the TOF measurement error, and the standard deviation of the brightness functions that is created by the misalignment distributions of the neutron guide. The open circles are the grand average of all 300 brightness functions shown in Fig. 6 combined (via Eq. (21)), with uncertainties given by Eq. (24). This curve represents a “typical” brightness function, averaging differences observed between the three measurements that may constitute real spectrum changes over the course of a reactor cycle. The black diamond symbols are the results of MCNP6 simulations in which the liquid hydrogen is given an ortho: para ratio of 17.5%: 82.5%. For reference, the extremes of the MCNP6 simulations (100% para – dashed line and 75% ortho [normal hydrogen] solid line) are also plotted. Other simulated o- p ratios are omitted for reasons of clarity.

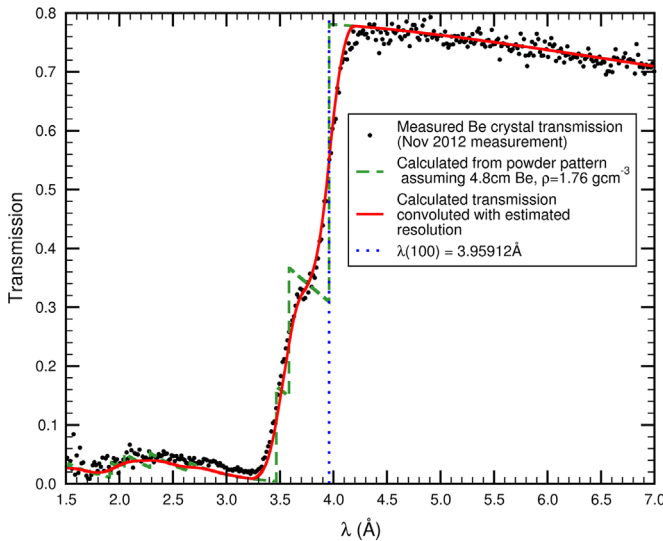


Fig. 8. From the theoretical Be powder transmission curve (dashed curve), the position of the (100) edge (dotted line) associated with $\lambda=3.959\text{ \AA}$ is clearly identified. The theoretical powder pattern was convoluted with the estimated (chopper) resolution function (see Appendix B) to produce the bold curve. By horizontally shifting the bold curve until it best matches the features in the measured spectrum (circular points), we identify accurately the position of $\lambda(100)$ in the measured data.

change in o- p ratio. Changes on the short wavelength edge of the spectral peak are sensitively correlated with the assumed reflectivity of the neutron guide and with angular misalignments, which are obtained from unique random samples for each data set. As mentioned in Sections 1 and 5, this sensitivity is caused by the transmission behavior of long curved neutron guides, which exhibits a rapid

Table 1

Solutions for the neutron effective flight path length, $\langle D \rangle$, and the “zero channel” delay, δ , from the three TOF measurements. Since the TOF trigger signal was passed through an adjustable delay module, a different time shift (and corresponding value of δ) was observed for each measurement. The distribution of $\langle D \rangle$ values is not truly understood, but may be indicative of varying degrees of disoriented layers of non-graphitic carbon [32,34] throughout the graphite crystal, yielding a range of $d(002)$ values, depending on the part of the crystal that is illuminated.

Measurement	October 24, 2012	November 3, 2012	December 3, 2012
$\langle D \rangle$ (mm)	851.8	855.4	861.0
δ (μs)	103.48	177.12	203.40

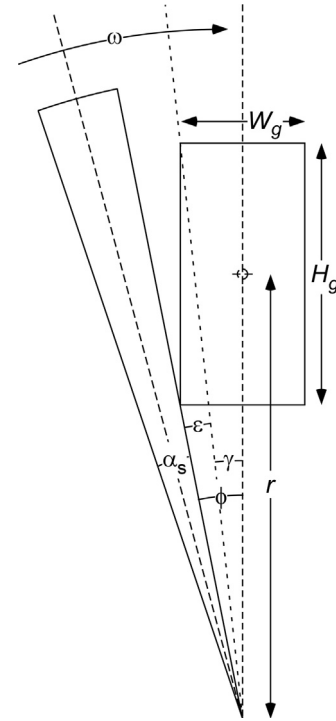


Fig. 9. A tall radial shopper slot of angular width α_s rotating at angular speed ω traversing a centered neutron guide or slit of width W_g , height H_g , whose center is a distance r from the axis of rotation.

drop off below a certain wavelength. Small changes in the reflectivity or alignment cause the position of the transmission edge to wander, with a consequently increased standard deviation of the results in this region. Even though the separate measurements at short wavelength differ by about 2 standard deviations of the apparent influence of the simulated guide misalignments (see Fig. 6), low counting statistics and the precise degree of background subtraction are factors that significantly affect the inferred brightness computation below about 1.5 \AA wavelength. Since the background subtraction was assessed independently for each measurement, inferred brightness fluctuations of this order could easily occur. Therefore, appropriate caution should be exercised in attributing great significance to spectral variations at the short wavelengths. Additional variations in the reactor core during a cycle, such as fuel distribution and control arm position, could potentially influence the flux distribution around the cold source and, consequently, the cold neutron spectrum that emerges. Study of these as-yet unquantified influences requires reactor models appropriate for the different degrees of fuel burn-up.

The attempt to measure a spectral shift associated with a radiation-induced increase in ortho- H_2 content immediately after startup (December measurement) failed to show a statistically significant change on the time scale of the measurements, despite

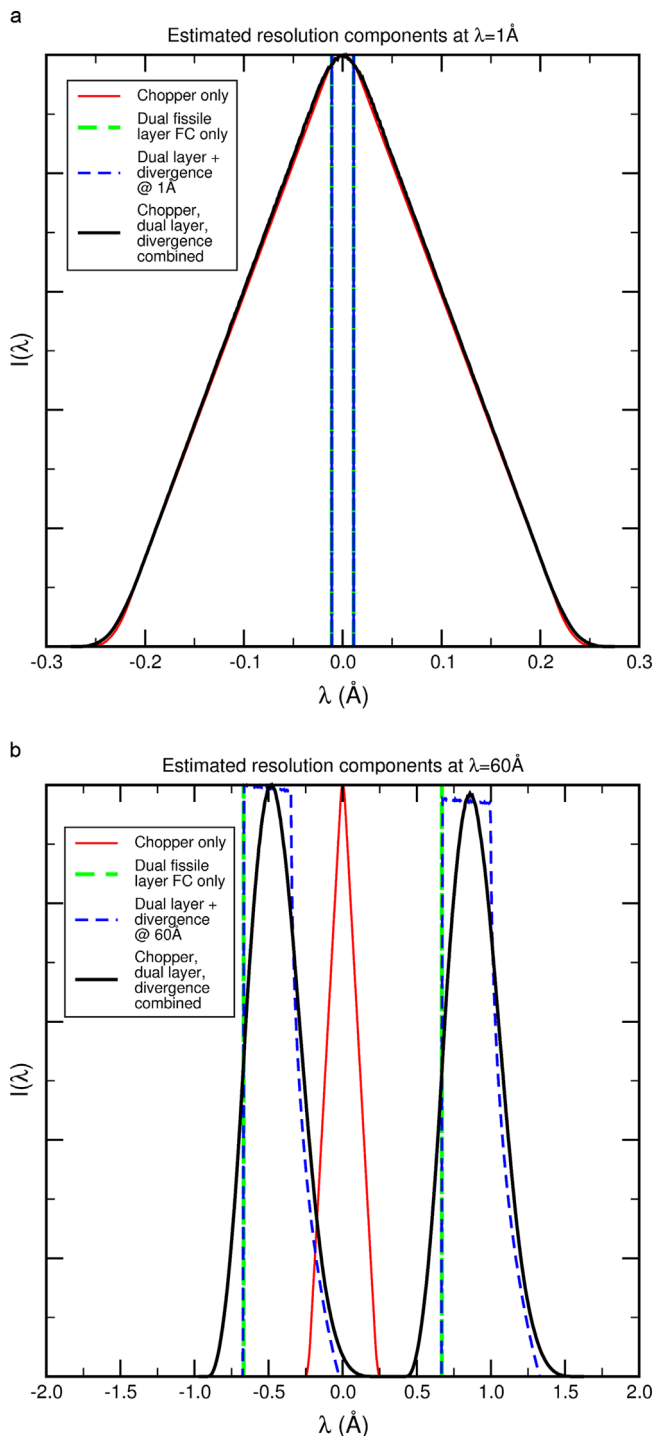


Fig. 10. Simulated components of the experimental resolution at $\lambda=1\text{\AA}$ (a) and at $\lambda=60\text{\AA}$ (b): Fine solid curve: Chopper only; bold dashed curve: Dual fissile layer of detector only; fine dashed curve: Dual fissile layer with divergence corresponding to an all-Ni-coated neutron guide at wavelength λ ; bold solid curve: Combination of all resolution components. Note that the chopper resolution dominates at short wavelength.

an attempt to maximize the para content prior to startup. A number of challenges posed limitations on this measurement: (i) There was no possibility of measuring the para hydrogen content prior to startup; (ii) the Unit 2 cold source of the NBSR does not employ catalysis to accelerate growth of the para content and the presence of high levels of decay radiation in the reactor core at shutdown may further hamper any deliberate attempt to achieve it; (iii) the ramp up of reactor power prior to opening of the beam is far from

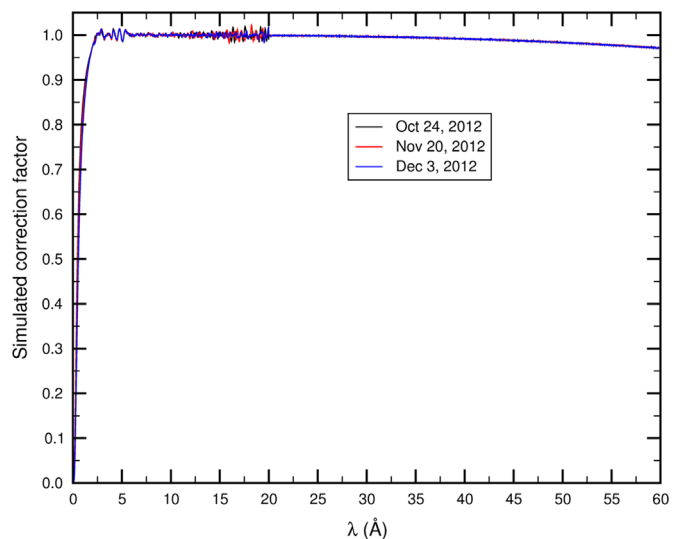


Fig. 11. The simulated resolution "correction function" (multiplier of resolution-broadened data) to make a first order correction of the measured spectrum for resolution effects. The smoother part for $\lambda > 20\text{\AA}$ results from fitting the noisier part of the measured $d\phi_e/d\lambda$ with a smooth function. In the resolution correction process, the entire curve above 6.4\AA was replaced by a quadratic fit function in order to minimize the transfer of statistical fluctuations.

instantaneous ($\approx 30\text{ min}$), during which the cold source is exposed to elevated levels of radiation; (iv) the time-of-flight measurements required a minimum count time of about ten minutes in order to achieve sufficient statistics to compare consecutively measured spectra reliably; (v) the apparent equilibrium ortho- H_2 level indicated by the present study is not large to start with and the initial state of the liquid hydrogen, given the slow uncatalyzed conversion, may not have differed greatly from its equilibrium state. Nonetheless, we can conclude that no significant change in the spectrum was observed on the time scale between 30 min to several hours following startup with liquefied hydrogen that was allowed to convert naturally towards its ground state for some days prior to startup. Unfortunately, an independent assessment of the isomeric composition of the liquid hydrogen was not feasible at the time of the present measurements. Instead, it has been inferred from our remote measurement of the spectrum emitted through a shell-like liquid hydrogen geometry, which has a weaker composition dependence than is observed from near-100% para, thick target transmission measurements below 15 meV neutron energy [26]. In the latter, even the smallest introduction of ortho- H_2 leads to a significant attenuation. The reduced o- p ratio dependence in our situation is also apparent from examination of the extremes of the MCNP simulations (see 100% para – dashed line and 75% ortho – solid line shown in Fig. 7). We have a reasonable degree of confidence in the ortho and para scattering kernels of our MCNP simulations, since calculations using previous generations of (discrete) ENDF/B-V and ENDF/B-VI ortho and para scattering kernels successfully reproduce measurements on a liquid hydrogen moderator system in which the o- p ratio was verified experimentally [27]. This likely leaves the accuracy of the liquid hydrogen density distribution as the dominant factor influencing the inferred o- p ratio. The largest systematic discrepancy between the measurements and the MCNP simulations (observed for all simulated o- p ratios) is found in the wavelength range from about 3\AA to 5\AA ($\approx 3\text{ meV}$ to 9 meV), where the MCNP simulations consistently overestimate the intensity. This is partly because MCNP insufficiently accounts for Bragg scattering from in-beam materials owing to the unavailability or inadequacy of $S(\alpha,\beta)$ thermal neutron scattering data for most materials. For the Al6061 alloy components of the model (including the cold source windows), the simulation uses ENDF/B-VII.0 $S(\alpha,\beta)$ data for pure aluminum as

an approximation. The $S(\alpha, \beta)$ includes coherent or incoherent elastic scattering (but not both) as well as thermal diffuse scattering. The pure aluminum $S(\alpha, \beta)$ data used were al27.22t (293.6 K) for the room temperature Al6061 components and al27.20t for the liquid hydrogen-temperature (20 K) components, both of which contain the coherent elastic scattering data; however no $S(\alpha, \beta)$ data was available for other materials in the MCNP model. The (200) and (111) Bragg edges from the aluminum account for the steps that are nominally located at about $\lambda=4.05 \text{ \AA}$ and about 4.67 \AA ; however, comparison of the $S(\alpha, \beta)$ with measurements for Al6061 in transmission geometry reveal that the pure aluminum $S(\alpha, \beta)$ is likely to over-estimate the transmission in these regions. This is confirmed by the depth of aluminum Bragg edge dips that are observed on other instruments around the NCNR facility, which are consistently underestimated when using the available $S(\alpha, \beta)$. The MCNP tally binning, which is chosen sufficiently coarsely to preserve statistics, inevitably washes out the Bragg features to some extent. Nonetheless, the discrepancy between the measurement and the MCNP simulation in this region appears to be a true one, since the “hollow” in the measured brightness curve cannot be removed even when divided by the combined materials transmission included in the analysis of the measurements. (Note that the latter was performed using lower transmission, *measured* Al6061 data.) Therefore, the hollow observed in all measurements cannot be entirely attributed to Bragg scattering correction issues.

Finally, some significant discrepancies have been observed between ortho hydrogen kernels originating from the ENDF/B-VII library and data prepared by the Institut für Kernenergetik und Energiesysteme (IKE), University of Stuttgart [28]. In this work, the MCNP simulations have used the latest continuous energy cross-sections and liquid hydrogen scattering kernels (hortho.20t, hpara.20t) from the ENDF/B-VII.0 (ENDF71SaB library). We cannot conclusively test the validity of one data set over the other because of the uncertainty in the ortho: para hydrogen ratio and in the exact hydrogen density distribution. A recent review of the liquid hydrogen scattering kernel calculations by the Los Alamos and IKE groups reveals approximations particular to each [29]. However, using the ENDF B-VII kernel set, we do observe that the main features of the measured brightness spectrum are well described near the median of the family of curves simulated in the range between 100% para and normal (25% para) hydrogen at 20 K. A significant effort is currently underway to improve neutron cross-section calculations (including those for liquid hydrogen) under the Work Package 11 (WP11 – Instruments & Experiments: Enhancement of neutron beams) research program of the CRISP initiative [30], for which an initial report has been released [31]. Ultimately, improved kernels will be incorporated into the transport calculations as they become available.

Disclaimer

Certain commercial entities, equipment, or materials may be identified in this document in order to describe an experimental procedure or concept adequately. Such identification is not intended to imply recommendation or endorsement by the National Institute of Standards and Technology, nor is it intended to imply that the entities, materials, or equipment are necessarily the best available for the purpose.

Acknowledgments

The authors wish to thank George Baltic, Mike Rinehart, Doug and Danny Ogg for invaluable technical support. We would also like to thank Christian Schanzer of Swiss Neutronics AG, Switzerland, for provision of technical data relating to the guide NG-Bu,

Brian Maranville, Brian Kirby, Chuck Majkrzak, Scott Dewey, and Terry Udovic for loan of equipment, and Antonio Faraone, John Copley, and Dan Adler for useful discussions. Finally, we wish to thank Sean O’Kelly, NCNR Reactor Operations, and NCNR Health Physics for their cooperation.

Appendix A. Wavelength and flight path length calibration

In general “time zero” of the TOF spectrum does *not* correspond to $\lambda=0 \text{ \AA}$. In order to calibrate the 0 \AA position and *actual* wavelength channel width (requiring a precise measurement of D), the positions of the [100] and [002] powder transmission edges from polycrystalline Be and graphite respectively were used as references. The assumed d -spacings were 1.97956 \AA and 3.38405 \AA , respectively. The latter value implies a proportion of disoriented layers, p , as defined by Franklin [32], (Eq. (1) in this reference) of about 0.59, but gave solutions for D that were close to those predicted by manual measurement of the flight path length. $d=3.38405 \text{ \AA}$ represents an approximately 0.9% increase with respect to the “perfect” room temperature Bernal structure [33] value and corresponds to about 4 channels in our TOF spectrum. With a radial chopper slot opening angle of 1.36° (mean radius 41.91 mm) and a 1 mm rectangular beam-defining slit, the estimated wavelength resolution (chopper only approximation – see Appendix C and B) is about 0.235 \AA FWHM (≈ 15.5 channels), which broadens the (otherwise vertical) transmission edges considerably. In order to facilitate the accurate location of these features, two theoretical powder transmission patterns were calculated (with room temperature approximations for the thermal diffuse scattering and Debye–Waller factor): One with infinitely sharp resolution and one convoluted with the estimated experimental chopper resolution function. The calculated transmissions were translated over the measured transmission (taken as the normalized ratio of “with crystal” to “without crystal” measurements), plotted on a wavelength scale that was estimated by using the manually-measured value of $\langle D \rangle$. This is iterated until a good match of the convoluted curve with the data is obtained. In this way, the data channel corresponding to the reference wavelength is easily identified and the corresponding time in the unrotated TOF spectrum is assigned to the reference wavelength, $2d$. An example for the 4.8 cm -thick warm Be crystal measurement is shown in Fig. 8, showing a good agreement of the resolution-convoluted powder pattern (bold curve) with the measured data (circular points). The crossover of the abrupt edges in the deconvoluted theoretical powder pattern (dashed curve) with the resolution-broadened curve locates the reference wavelength in the latter more accurately. We now have two unknowns, the time delay, δ , between the chopper trigger and the 0 \AA time channel and the (approximately-known) mean flight path, $\langle D \rangle$. If the positions, $2d_1$ and $2d_2$, of the two reference powder edges in the raw time histogram are determined from the above procedure to be T_1 and T_2 respectively, we have

$$\begin{aligned} T_1 &= t_1 + \delta = \frac{2m_n d_1}{h} \langle D \rangle + \delta \\ T_2 &= t_2 + \delta = \frac{2m_n d_2}{h} \langle D \rangle + \delta \end{aligned} \quad (2)$$

therefore,

$$\begin{aligned} \langle D \rangle &= \frac{h}{2m_n} \frac{(T_2 - T_1)}{(d_2 - d_1)} \\ \delta &= T_1 - \frac{d_1}{(d_2 - d_1)}(T_2 - T_1) = T_2 - \frac{d_2}{(d_2 - d_1)}(T_2 - T_1) \end{aligned} \quad (3)$$

Because d_1 and d_2 are known with reasonable accuracy at the temperature of the measurement, we can solve for $\langle D \rangle$ and δ with the additional uncertainty that is associated with the

determination of T_1 and T_2 – in this case to the nearest $\frac{1}{2}$ channel width, corresponding to about 0.0075 \AA . In matrix notation:

$$\begin{bmatrix} \langle D \rangle \\ \delta \end{bmatrix} = \begin{bmatrix} 2d_1/(h/m_n) & 1 \\ 2d_2/(h/m_n) & 1 \end{bmatrix} \begin{bmatrix} T_1 \\ T_2 \end{bmatrix} \equiv \begin{bmatrix} \langle D \rangle \\ \delta \end{bmatrix} = \begin{bmatrix} 2d_1/(h/m_n) & 1 \\ 2d_2/(h/m_n) & 1 \end{bmatrix}^{-1} \begin{bmatrix} T_1 \\ T_2 \end{bmatrix} \quad (4)$$

where “ \equiv ” implies left division. The results for the three measurements are summarized in Table 1.

Appendix B. Estimate of chopper resolution function

The chopper has a radial slot crossing a centered, rectangular neutron source as illustrated in Fig. 9. From Fig. 9, we define $r_1 = r - H_g/2$, $r_2 = r + H_g/2$, $\tan \gamma = W_g/2r_2$, $\tan \phi = W_g/2r_1$, $\varepsilon = \phi - \gamma$, and the source area $A_g = W_g H_g$. The total duration for neutron transmission through the slot from start to finish is

$$\tau_{tot} = \frac{2\phi + \alpha_s}{\omega} \quad (5)$$

It is simple to treat the transmission function of the chopper slot by considering the open guide area traced out behind the leading edge of the slot, then subtract the similar function shifted in angle by $-\alpha_s$ for the trailing edge of the slot. First we define the following times for the leading edge of the slot within the limits of the duration of the pulse: $t_0 = -\phi/\omega$, $t_1 = -\gamma/\omega$, $t_2 = 0$, $t_3 = \gamma/\omega$, $t_4 = \phi/\omega$, $t_5 = (\phi + \alpha_s)/\omega$, so that the area of the source traced out behind the leading edge of the slot, A_1 , is given by:

$$A_1(t < t_0) = 0 \quad (6)$$

$$A_1(t_0 \rightarrow t_1) = \frac{(W_g - 2r_1 \tan |\omega t|)^2}{8 \tan |\omega t|} \quad (7)$$

with $A_1(t_1) = A_g H_g / 4r_2$.

$$A_1(t_1 \rightarrow t_2) = \frac{1}{2} A_g - r H_g \tan |\omega t| \quad (8)$$

with $A_1(t_2) = A_g / 2$.

$$A_1(t_2 \rightarrow t_3) = \frac{1}{2} A_g + r H_g \tan \omega t \quad (9)$$

with $A_1(t_3) = \frac{1}{2} A_g (1 + r/r_2)$.

$$A_1(t_3 \rightarrow t_4) = A_g - \frac{(W_g - 2r_1 \tan \omega t)^2}{8 \tan \omega t} \quad (10)$$

with $A_1(t_4) = A_g$. Finally,

$$A_1(t > t_4) = A_g \quad (11)$$

The chopper pulse shape is then calculated from the function

$$f(t) = A_1(t) - A_1(t - \alpha_s/\omega); \quad t = t_0 \rightarrow t_5 \quad (12)$$

Appendix C. Resolution contributions and correction

There are three principal resolution contributions affecting the measurements:

1. The neutron time-of-flight uncertainty due to the non-zero chopper pulse duration – see Appendix B (wavelength uncertainty independent of wavelength).
2. A discrete flight path length uncertainty due to the physical separation of the dual fissile coatings of the fission chamber detector (wavelength uncertainty approximately proportional to wavelength).
3. Neutron flight path length uncertainty due to beam divergence (wavelength uncertainty approximately proportional to wavelength).

The first of these contributions is wavelength-independent and dominates at short wavelengths (short times of flight). This is because the chopper pulse duration is an increasing fraction of the time-of-flight as λ (or TOF) $\rightarrow 0$. The full width at half maximum (FWHM) of the wavelength uncertainty is obtained from the FWHM of the chopper pulse width in time via

$$\Delta\lambda_{FWHM,chop}(\lambda) \approx \frac{h}{m_n} \frac{\Delta t_{FWHM,chop}}{\langle D \rangle}$$

where $\langle D \rangle$ is the separation of the chopper and the mid-plane of the two active layers of the fission chamber. The experimental parameters are (see notation in Appendix B), $r = 41.9 \text{ mm}$, $\alpha = 1.36^\circ$, $W_g = 1 \text{ mm}$, $H_g = 12.7 \text{ mm}$, $\omega = 0.472 \text{ mrad}/\mu\text{s}$, which, from Eq. (5), gives $\Delta t_{FWHM,chop} \approx \tau_{tot}/2 \approx 54.9 \mu\text{s}$. Using the mean measured $\langle D \rangle$ from Table 1 $\approx 856.1 \text{ mm}$, we have $\Delta\lambda_{FWHM,chop} \approx 0.254 \text{ \AA}$ due to the chopper at all wavelengths.

The second effect produces a dual peak resolution function with peak separation (in wavelength) $\Delta\lambda_{FC} = \lambda \delta_{FC} / \langle D \rangle$, where δ_{FC} is the physical separation of the fissile layers. Here, we have $\delta_{FC} = 19.1 \text{ mm}$. If $\langle D \rangle = 856.1 \text{ mm}$ then $\Delta\lambda_{FC} \approx \pm 0.0112\lambda$. For $\lambda = 1 \text{ \AA}$, this separation is only about 8.8% of $\Delta\lambda_{FWHM,chop}$, so the dual peak is not resolved in the convolution, whereas at $\lambda = 60 \text{ \AA}$, the peak separation is 5.27 times greater than $\Delta\lambda_{FWHM,chop}$. For a perfectly collimated beam, this causes the resolution function to appear as two well-separated chopper resolution functions centered at 59.33 \AA and 60.67 \AA .

Finally, the beam divergence-dependence of the resolution arises from the distribution of flight path lengths resulting from the divergence of neutron trajectories allowed through the instrumental collimation. In the present case, this is more or less the beam divergence emitted from a long natural nickel-coated neutron guide. The latter may be approximated by uniformly random horizontal and vertical beam divergence within the limits $\pm \theta_c$, where θ_c is the critical angle of reflection with $\theta_c \approx 1.73 \times 10^{-3} \lambda (\text{\AA})$ rads for Ni. In the small angle approximation, it can be shown analytically that the mean polar angle of such a distribution is given by

$$\langle \theta \rangle = \frac{\sqrt{2}}{3} \left[1 + \frac{1}{\sqrt{32}} \ln \left(\frac{3+2\sqrt{2}}{3-2\sqrt{2}} \right) \right] \theta_c \approx 0.765\theta_c$$

Using $\langle \theta \rangle$ as a typical angular deviation of the neutron trajectory with respect to the beam axis ($\theta = 0$), we have

$$\Delta\lambda_{div} \approx \frac{\Delta D}{\langle D \rangle} \lambda \approx \frac{\langle \theta \rangle^2}{2} \lambda \approx 8.75 \times 10^{-7} \lambda \left[\frac{\text{\AA}}{\text{\AA}} \right]^3 \quad (13)$$

where we have used the approximation $\cos \langle \theta \rangle \approx 1 - \langle \theta \rangle^2 / 2$, since $\langle \theta \rangle$ may be considered small, even at the longest wavelengths of interest. Clearly, at $\lambda = 1 \text{ \AA}$, $\Delta\lambda_{div}$ is negligible; however, at $\lambda = 60 \text{ \AA}$, Eq. (13) yields $\Delta\lambda_{div} \approx 0.19 \text{ \AA}$ (about 13 channel widths in our experimental setup [see Section 3]).

These components are simulated and illustrated in Fig. 10 for $\lambda = 1 \text{ \AA}$ (a) and $\lambda = 60 \text{ \AA}$ (b). Clearly, the resolution function cannot be approximated by the chopper resolution at long wavelengths. Even if the resolution function were simple and wavelength-independent, attempts at deconvolution are fraught with potential errors and the result is highly sensitive to noise in the data. The complex wavelength-dependence of the resolution also means that a “forward” method, such as convoluting the resolution function with the (resolution-broadened) data, multiplied by a suitable fit function representing the effect of deconvolution, and least squares fitting to the original data, is also impractical. The latter also relies on choosing a realistic “resolution correction” function. Instead, the following procedure was adopted.

The background-corrected, resolution-broadened $1/\nu$ data (i.e., what is actually measured by the fission chamber) was used as a first-order approximation to the deconvoluted data. Some smoothing

was required to reduce sensitivity of the procedure to noise (just as with numerical convolution or FFT deconvolution). A Savitzky–Golay filter with polynomial order 2 and a left and right frame of 7 channels gave excellent smoothing of channel-to-channel noise fluctuations without eliminating the real structure of the data. The shortest ($\lambda < 2.2 \text{ \AA}$) and longest ($\lambda > 20 \text{ \AA}$) wavelengths were also fitted by smooth functions that describe well the continuous curvature in these regions to reduce noise sensitivity (hence the smoother regions in Fig. 11). The effects of resolution were then explored by using Monte Carlo selection of the resolution components:

- (i) The effect of the chopper transmission (by picking a weight according to the start time distribution, as calculated above).
- (ii) The effect of the dual fissile layer by randomly picking one plate or the other to define the flight path length $D = \langle D \rangle \pm \delta_{FC}/2$. A 50:50 sampling provides a good approximation because both fissile layers are nominally equivalent and highly transmitting.
- (iii) The effect of beam divergence (by randomly picking a horizontal trajectory component, θ_x , within $\pm \theta_c(\text{Ni})$, then a vertical component, θ_y , within $\pm \theta_c(\text{Ni})$ and calculating the polar angle $\theta = \sqrt{\theta_x^2 + \theta_y^2}$). The flight path length is then $D/\cos \theta$.

The resolution “correction” is obtained approximately by taking the ratio of the simulated data to the original. These functions for the three measurements of $d\varphi_c/d\lambda$ are illustrated in Fig. 11. The oscillations up to about 5.5 \AA appear to be real artifacts of the peaks/dips in the data, some of which occur due to adjacent structure such as Bragg edges from aluminum. Above about 6.4 \AA , the function shows only features consistent with statistical fluctuations and is well described by a quadratic function (which was applied in the data correction). The success of this first order correction was verified for the shorter wavelengths (where the resolution function is well approximated by the chopper resolution function) by convoluting the corrected data with the chopper resolution function and comparing with the original data. The resulting ratio, which was centered statistically about 1.0 indicated that the resolution correction was successful.

Appendix D. Treatment of uncertainties

Each measurement date produced a *slightly different spectrum*. Since some care was taken to avoid perturbation of the experimental setup between measurements, this may indicate a small, but real, spectral shift. The standard deviation of the combined results of the three measurements becomes an estimate of the “systematic” error associated either with real spectral changes during a reactor cycle, or else the imprecision/irreproducibility of the measurement. The interpretation is irrelevant for the purposes of producing a mean spectrum with estimated uncertainties.

The three TOF measurements produced three 20 MW-normalized $d\varphi_c/d\lambda$ curves, with error bars propagated from the TOF analysis. These originate from the propagated TOF counting statistics when producing the background-corrected “ $1/\nu$ ” data and the uncertainty, Δf_{norm} , in the spectrum normalization factor, f_{norm} . The uncertainty in the spectrum normalization is the combination of the capture flux uncertainty from the gold foil analysis (about $\pm 1.4\%$, dominated by the foil irradiation time uncertainty, rather than decay counting statistics [$\approx 0.2\%$]) and the estimated uncertainty on the numerical integration of the TOF thermal-equivalent spectrum integral (which turns out to be small compared to the Au foil measurement uncertainty). Since the capture flux (φ_c) normalization is applied as a wavelength-independent constant factor on the whole $1/\nu$ spectrum, the constant $\Delta f_{norm}/f_{norm}$ is added in quadrature to the statistical count error of each TOF bin to

produce the overall error bar for each wavelength bin of $d\varphi_c/d\lambda$. After multiplying $d\varphi_c/d\lambda$ and the corresponding errors by λ_{2200}/λ , where λ_{2200} is the wavelength of a neutron traveling at 2200 ms^{-1} ($\approx 1.798 \text{ \AA}$), we obtain the inferred $d\varphi/d\lambda$ spectra, shown for the three measurements in Fig. 4. Since only one Au foil measurement (performed Oct 11, 2012 at the reactor startup) normalizes all three measurements, there is an unknown (but presumably small) uncertainty on f_{norm} associated with possible changes in the capture flux with degree of fuel burnup. There are the additional possibilities that the neutron flux spectrum within the centered $0.2''$ diameter gold foil differs from that at the position of the chopper slot and that the flux near the guide center differs from the average over the guide cross-sectional area. The former is likely to be negligible since the chopper slot was also centered on the cross-sectional area of the guide. The latter may be more significant. However, these additional uncertainties are assumed to fall within the relatively large (1.4%) uncertainty of the gold foil measurement itself and are henceforth ignored. Spectrum “abscissa” uncertainties (due to wavelength calibration errors) are harder to estimate and have the intrinsic half-channel width uncertainty of the original TOF data. There is an unavoidable uncertainty in the d -spacings of the crystal reference materials (particularly for the graphite – see Appendix A), used for the wavelength calibration. There is also some uncertainty in the determination of their powder Bragg edges due to resolution effects, which was minimized by using the estimated chopper resolution function, as described in Appendix A. The wavelength calibration uncertainty is ignored, other than any left-right fluctuation is somewhat smeared when combining the results of the three measurements, for which three independent calibrations were performed.

The second aspect of the uncertainty concerns that of the source brightness (B) determination using the measured $d\varphi/d\lambda$ curves, mentioned above, and the additional uncertainty from the simulation of the neutron guide transmission. As mentioned in the text, the effect of guide misalignments is estimated from the standard deviation of the simulation results of 100 random configurations chosen from the assumed distributions. The effect of the uncertainty of the guide reflectivity is assumed small since the model is based on measurements, as described in the text. The simulations were performed so that the Monte Carlo statistics (the standard deviation of the *mean* guide transmission, $\langle T_{jk} \rangle$, as determined from the mean neutron weight at the guide exit evaluated over a number of histories, i , for each wavelength j of each simulation, k), given in the limit of a large number of histories, N_{jk} , by:

$$S_{MC}(\langle T_{jk} \rangle) = \sqrt{\frac{\sum_{i=1}^{N_{jk}} (T_{jik} - \langle T_{jk} \rangle)^2}{N_{jk}(N_{jk} - 1)}} \quad (14)$$

is small compared with the intrinsic error on the mean brightness evaluated at wavelength j , $\langle B_j \rangle$, associated with the TOF measurement error, $\delta d\varphi/d\lambda_j$ on the measurement $d\varphi/d\lambda_j$:

$$\delta \langle B_j \rangle_M = \langle B_j \rangle_M \left[\frac{\delta(d\varphi/d\lambda_j)}{d\varphi/d\lambda_j} \right]_M \quad (15)$$

where M labels the measurement (i.e., October, November, or December, as appropriate). The condition $S_{MC}(\langle T_{jk} \rangle) \ll \delta \langle B_j \rangle_M$ is ensured by running a sufficiently large number of histories, N_{jk} , for each wavelength λ_j in each simulation k . Nonetheless, the displayed error on $\langle B_j \rangle$ does include the Monte Carlo statistical term, $S_{MC}(\langle T_{jk} \rangle)$, for each simulation, k , via

$$\Delta \langle B_j \rangle_{Mk} = \langle B_j \rangle_{Mk} \sqrt{\left[\left(\frac{\delta(d\varphi/d\lambda_j)}{d\varphi/d\lambda_j} \right)_M^2 + \left(\frac{S_{MC}(\langle T_{jk} \rangle)}{\langle T_{jk} \rangle} \right)_k^2 \right]} \quad (16)$$

These are the error bars that appear on the individual simulation curves in Fig. 6.

Finally, we wish to produce averaged brightness curves from the multiple simulations (100 per measurement date for the three measurement dates [300 curves total] that are represented in Fig. 6). We may produce the average for a given measurement date (average of 100 simulations), the grand average of all measurements (average of 300 simulations), or even the average of the measurement date averages (average of three individually-averaged curves). In evaluating these averages, we wish to combine the error bars on the individual simulation curves ([Eq. (16)]) with the appropriate estimated standard deviation of the simulation curves. The latter, for a sufficiently large sample, accounts approximately for the distribution in brightness values that is attributable to the distribution of guide misalignments. For instance, if N_M is the total number of simulations for measurement M (in this case 100), the weighted mean brightness at wavelength j of measurement M , averaged over the N_M simulations, is

$$\langle B_j \rangle_M = \frac{\sum_{k=1}^{N_M} (\langle B_j \rangle_{Mk} / \Delta \langle B_j \rangle_{Mk}^2)}{\sum_{k=1}^{N_M} (1 / \Delta \langle B_j \rangle_{Mk}^2)} \quad (17)$$

with an uncertainty in the weighted mean due to the error bars on the individual simulation curves given by

$$\sigma_1(\langle B_j \rangle_M) = \frac{1}{\sqrt{\sum_{k=1}^{N_M} (1 / \Delta \langle B_j \rangle_{Mk}^2)}} \quad (18)$$

However, we are not finished, since we also wish to combine the standard deviation of the simulated $\langle B_j \rangle_{Mk}$ associated with the guide misalignments; this is given by:

$$\sigma_2(\langle B_j \rangle_M) = \sqrt{\frac{1}{N_M - 1} \sum_{k=1}^{N_M} (\langle B_j \rangle_{Mk} - \langle B_j \rangle_M)^2} \quad (19)$$

where $\langle B_j \rangle_M$ is given by Eq. (17). Finally, we obtain the estimated error bar on the mean brightness derived from TOF measurement M from:

$$\Delta \langle B_j \rangle_M \approx \sqrt{\sigma_1(\langle B_j \rangle_M)^2 + \sigma_2(\langle B_j \rangle_M)^2} \quad (20)$$

These are the error bars shown on the individual October, November, and December points shown in Fig. 7.

When combining all the simulations for all measurements M (i.e., all 300 simulations), we are performing an additional summation over M , i.e.,

$$\langle B_j \rangle = \frac{\sum_M \sum_{k=1}^{N_M} (\langle B_j \rangle_{Mk} / \Delta \langle B_j \rangle_{Mk}^2)}{\sum_M \sum_{k=1}^{N_M} (1 / \Delta \langle B_j \rangle_{Mk}^2)} \quad (21)$$

with

$$\sigma_1(\langle B_j \rangle) = \frac{1}{\sqrt{\sum_M \sum_{k=1}^{N_M} (1 / \Delta \langle B_j \rangle_{Mk}^2)}} \quad (22)$$

and

$$\sigma_2(\langle B_j \rangle) = \sqrt{\frac{1}{N_{tot} - 1} \sum_M \sum_{k=1}^{N_M} (\langle B_j \rangle_{Mk} - \langle B_j \rangle)^2} \quad (23)$$

where $N_{tot} = \sum_M N_M$. Finally,

$$\Delta \langle B_j \rangle \approx \sqrt{\sigma_1(\langle B_j \rangle)^2 + \sigma_2(\langle B_j \rangle)^2} \quad (24)$$

These are the error bars shown on the open circles in Fig. 7.

If, instead, we are calculating the average of the averages for each of the M measurements, we have

$$\langle \bar{B}_j \rangle = \frac{\sum_M (\langle B_j \rangle_M / \Delta \langle B_j \rangle_M^2)}{\sum_M (1 / \Delta \langle B_j \rangle_M^2)} \quad (25)$$

with $\langle B_j \rangle_M$ and $\Delta \langle B_j \rangle_M$ given by Eqs. (17) and (20), respectively, and

$$\sigma_1(\langle \bar{B}_j \rangle) = \frac{1}{\sqrt{\sum_M (1 / \Delta \langle B_j \rangle_M^2)}} \quad (26)$$

and

$$\sigma_2(\langle \bar{B}_j \rangle) = \sqrt{\frac{1}{M-1} \sum_M (\langle B_j \rangle_M - \langle \bar{B}_j \rangle)^2} \quad (27)$$

where $\langle \bar{B}_j \rangle$ is given by Eq. (25).

References

- [1] J. Butterworth, P.A. Egelstaff, H. London, F.J. Webb, *Philosophical Magazine* 2 (1957) 917.
- [2] S.J. Cocking, F.J. Webb, *Neutrons sources and detectors*, in: P.A. Egelstaff (Ed.), *Thermal Neutron Scattering*, Academic Press, London and New York, 1965.
- [3] D. Cribier, B. Jacrot, A. Lacaze, and P. Roubeau, *Expérience de Thermalisation de Neutrons Lents par de l'Hydrogène Liquide*, in: *Inelastic Scattering of Neutrons in Solids and Liquids*, Proceedings of the Symposium on Inelastic Scattering of Neutrons in Solids and Liquids, IAEA, Vienna, 1961.
- [4] B. Jacrot, *Pile Neutron Research in Physics*, IAEA, Vienna (1962) 393.
- [5] A. W. McReynolds and W. L. Whittemore, *Inelastic Scattering of Neutrons from Very Cold Materials*, in: *Inelastic Scattering of Neutrons in Solids and Liquids*, Proceedings of the Symposium on Inelastic Scattering of Neutrons in Solids and Liquids, IAEA, Vienna, 1961.
- [6] P. Ageron, Ph. De Beaucourt, H.D. Harig, A. Lacaze, M. Livolant, *Cryogenics* 9 (1969) 42.
- [7] P. Ageron, *Nuclear Instruments and Methods in Physics Research Section A* 284 (1989) 197.
- [8] W. Gaubatz, K. Gobrecht, *Physica B* 276–278 (2000) 104.
- [9] S.J. Kennedy, *Physica B* 385–386 (2006) 949.
- [10] P. Kopetka, R.E. Williams, J.M. Rowe, *NIST Liquid Hydrogen Cold Source NIST Internal Report NISTIR 7352*, , 2006.
- [11] T. Kai, M. Harada, M. Teshigawara, N. Watanabe, Y. Kiyonagi, Y. Ikeda, *Nuclear Instruments and Methods in Physics Research Section A* 550 (2005) 329.
- [12] K. Batkov, A. Takibayev, L. Zanini, F. Mezei, *Nuclear Instruments and Methods in Physics Research Section A* 729 (2013) 500.
- [13] MCNP6.1, Monte Carlo Codes (XCP-3), X Computational Physics Division, System Design & Analysis (NEN-5), Nuclear Engineering & Nonproliferation Division, Los Alamos National Laboratory, May, 2013.
- [14] M.B. Chadwick, P. Obložinský, M. Herman, N.M. Greene, R.D. McKnight, D.L. Smith, P.G. Young, R.E. MacFarlane, G.M. Hale, S.C. Frankle, A.C. Kahler, T. Kawano, R.C. Little, D.G. Madland, P. Moller, R.D. Mosteller, P.R. Page, P. Talou, H. Trellue, M.C. White, W.B. Wilson, R. Arcilla, C.L. Dunford, S.F. Mughabghab, B. Pritychenko, D. Rochman, A.A. Sonzogni, C.R. Lubitz, T.H. Trumbull, J.P. Weinman, D.A. Brown, D.E. Cullen, D.P. Heinrichs, D.P. McNabb, H. Derrien, M.E. Dunn, N.M. Larson, L.C. Leal, A.D. Carlson, R.C. Block, J.B. Briggs, E.T. Cheng, H.C. Huria, M.L. Zerkle, K.S. Kozier, A. Courcelle, V. Pronyaev, S.C. van der Marck., *Nuclear Data Sheets* 107 (12) (2006) 2931.
- [15] J.D. Siegwarth, D.A. Olson, M.A. Lewis, J.M. Rowe, R.E. Williams, P. Kopetka, *Thermal Hydraulic Tests of a Liquid Hydrogen Cold Neutron Source NIST Internal Report NISTIR 5026*, , 1994.
- [16] J. Christ, T. Springer, *Nukleonik*, 4, 196223.
- [17] H. Maier-Leibnitz, T. Springer, *Journal of Nuclear Energy Part A/B* 17 (1963) 217.
- [18] F. Mezei, *Communications in Physics* 1 (1976) 81.
- [19] J.B. Hayter, H.A. Mook, *Journal of Applied Crystallography* 22 (1989) 35.
- [20] J.C. Cook, *Review of Scientific Instruments* 80 (2009) 023101.
- [21] C.J. Carlike, M.W. Johnson, W.G. Williams, *Neutron Guides on Pulsed Sources Rutherford Laboratory Report RL-79-084*, , 1979.
- [22] D.F.R. Mildner, *Nuclear Instruments and Methods in Physics Research Section A* 290 (1990) 189.
- [23] J.R.D. Copley, D.F.R. Mildner, *Nuclear Science and Engineering* 110 (1992) 1.
- [24] J. C. Cook, unpublished.

- [25] R. Ryan, Challenges of Neutron Guide Alignment at the NIST Center for Neutron Research, *Quality Digest*, August 22, 2011 (<http://www.qualitydigest.com/inside/quality-insider-article/challenges-neutron-guide-alignment-nist-center-neutron-research.html>).
- [26] L. Barron-Palos, R. Alarcon, S. Balascuta, C. Blessinger, J.D. Bowman, T.E. Chupp, S. Covrig, C.B. Crawford, M. Dabaghyan, J. Dadras, M. Dawkins, W. Fox, M. T. Gericke, R.C. Gillis, B. Lauss, M.B. Leuschner, B. Lozowski, R. Mahurin, M. Mason, J. Mei, H. Nann, S.I. Penttila, W.D. Ramsay, A. Salas-Bacci, S. Santra, P.-N. Seo, M. Sharma, T. Smith, W.M. Snow, W.S. Wilburn, V. Yuan., *Nuclear Instruments and Methods in Physics Research Section A* 659 (2011) 579.
- [27] M. Ooi, H. Ogawa, T. Kamiyama, Y. Kiyonagi, Experimental studies of the effect of the ortho/para ratio on the neutronic performance of a liquid hydrogen moderator for a pulsed neutron source, *Nuclear Instruments and Methods in Physics Research Section A* 659 (2011) 61.
- [28] R. E. Williams, M. Middleton, P. Kopetka, J. M. Rowe, and P. C. Brand, A liquid deuterium cold neutron source for the NIST research reactor – Conceptual Design presented at the Joint IGORR 2013 & IAEA Technical Meeting, Daejeon, Korea.
- [29] J. M. Rowe, private communication, 2013.
- [30] The Cluster of Research Infrastructures for Synergies in Physics: (<http://www.crisp-fp7.eu/about-crisp/>).
- [31] E. Guarini, The neutron cross section of the hydrogen liquids, CRISP – WP11: Moderator neutron cross-section data, Final Report on Cryogenic Liquids, Institut Laue-Langevin, Grenoble, 2014.
- [32] R.E. Franklin, *Acta Crystallographica* 4 (1951) 253.
- [33] J.D. Bernal, *Proceedings of the Royal Society of London A* 106 (1924) 749.
- [34] G.E. Bacon, *Acta Crystallographica* 4 (1951) 558.